Clim Dyn (2010) 35:771–784
DOI 10.1007/s00382-009-0612-x

Ocean–atmosphere coupling and the boreal winter MJO

Hye-Mi Kim · Carlos D. Hoyos · Peter J. Webster · In-Sik Kang

Received: 2 February 2009 / Accepted: 16 June 2009 / Published online: 28 June 2009

Abstract The influence of ocean–atmosphere coupling on the simulation and prediction of the boreal winter Madden–Julian Oscillation (MJO) is examined using the Seoul National University coupled general circulation model (CGCM) and atmospheric—only model (AGCM). The AGCM is forced with daily SSTs interpolated from pentad mean CGCM SSTs. Forecast skill is examined using serial extended simulations spanning 26 different winter seasons with 30-day forecasts commencing every 5 days providing a total of 598 30-day simulations. By comparing both sets of experiments, which share the same atmospheric components, the influence of coupled ocean–atmosphere processes on the simulation and prediction of MJO can be studied. The mean MJO intensity possesses more realistic amplitude in the CGCM than in AGCM. In general, the ocean–atmosphere coupling acts to improve the simulation of the spatio-temporal evolution of the eastward propagating MJO and the phase relationship between convection (OLR) and SST over the equatorial Indian Ocean and the western Pacific. Both the CGCM and observations exhibit a near-quadrature relationship between OLR and SST, with the former lagging by about two pentads. However, the AGCM shows a less realistic phase relationship. As the initial conditions are the same in both models, the additional forcing by SST anomalies in the CGCM extends the prediction skill beyond that of the AGCM. To test the applicability of the CGCM to real-time prediction, we compute the Real-time Multivariate MJO (RMM) index and compared it with the index computed from observations. RMM1 (RMM2) falls away rapidly to 0.5 after 17–18 (15–16) days in the AGCM and 18–19 (16–17) days in the CGCM. The prediction skill is phase dependent in both the CGCM and AGCM.

Keywords Ocean–atmosphere coupling · MJO · Prediction

H.-M. Kim (✉) · C. D. Hoyos · P. J. Webster
School of Earth and Atmospheric Science, Georgia Institute of Technology, 311 Ferst Dr., Atlanta, GA 30332, USA
e-mail: hyemi.kim@eas.gatech.edu

I.-S. Kang
School of Earth and Environmental Science, Seoul National University, Seoul, Korea

1 Introduction

The low-frequency intraseasonal oscillation (ISO), often referred to as Madden–Julian oscillation (MJO; Madden and Julian 1972, 1994), is a dominant mode of tropical variability accounting for a large percentage of convective variance in the tropics. The ISO/MJO is important because of its considerable influence on monsoon dynamics, generating active and break phases of convection during the South-East Asian and Australian monsoons, on general weather and climate variability and as an important part of the ENSO cycle (Lau and Chan 1986; Kang et al. 1989, 1999; Ferranti et al. 1990; Webster et al. 1998; Bergman et al. 2001; Han et al. 2001; Lawrence and Webster 2001, 2002; Jones et al. 2004a, b; Hoyos and Webster 2007; Kim et al. 2008a, among others). Overall, the ISO has a large impact on global medium- and extended-range forecast skill (Chen and Alpert 1990; Hendon et al. 2000; Jones and Schemm 2000; Webster and Hoyos 2004).

However, even the state-of-the-art dynamical models experience severe deficiencies representing the ISO/MJO with skillful forecasts only extending to 7–10 days (Chen and Alpert 1990; Lau and Chang 1992; Schemm et al.

1996; Jones et al. 2000; Seo et al. 2005). Recent observational and modeling studies have shown that the ocean–atmosphere coupling is crucial for the maintenance of the ISO/MJO. Furthermore, incorporating ocean–atmosphere coupling into a model improves the ISO/MJO simulation in terms of its activity, propagation characteristics, seasonality, and predictability (Waliser et al. 1999a; Woolnough et al. 2000; Webster et al. 2002; Fu et al. 2003; Fu and Wang 2004a, b; Rajendran et al. 2004; Rajendran and Kitoh 2006; Zheng et al. 2004; Fu et al. 2007; Woolnough et al. 2007; Kim and Kang 2008, among others).

Kim et al. (2008b, hereafter KHWK08) examined the influence of sea surface temperature (SST) on the simulation and predictability of the MJO using serial extended forecast integrations of the Seoul National University Atmospheric General Circulation Model (SNU AGCM). The serial runs were performed by prescribing observed SST with monthly, weekly and daily temporal resolutions and the results of the integrations illustrated that higher temporal SST resolution improves the simulation and potential predictability of the MJO intensity and eastward propagating characteristics. However, with an AGCM, the phase relationship between convection and SST becomes distorted as the forecast lead time increases even when using the daily SST. KHWK08 concluded that the explicit ocean–atmosphere coupled processes must be crucial for a better simulation and higher predictability of the MJO. This manuscript constitutes an extension of KHWK08, comparing extended forecasts performed with a Coupled GCM (CGCM) and an AGCM using a similar experimental framework.

Recently, Woolnough et al. (2007) examined the role of air–sea coupling on MJO forecasts using series of forecasts initialized daily for 47 days of the Tropical Ocean Global Atmosphere Coupled Ocean Atmosphere Response Experiment (TOGA-COARE) period. The study found an improvement of the MJO forecast skill by including ocean–atmosphere coupled processes. Fu et al. (2007), focusing on the summer ISO, also showed the inclusion of an interactive ocean significantly extended the theoretical limit of ISO predictability. In this paper, we also examine the differences and similarities of MJO simulation and prediction between coupled and atmospheric-only models. However, this work has significant differences to earlier studies.

The first distinctive difference is the focus on the practical prediction skill rather than the potential predictability of the ISO/MJO. Several studies have indicated the importance of ocean–atmosphere coupling on the ISO/MJO prediction for both summer and winter (Fu et al. 2007; Pegion and Kirtman 2008). For example, Fu et al. (2007) focused on the impact of ocean–atmosphere coupling and SST variability on potential predictability for boreal summer ISO using series of twin perturbation experiments for selected events relative to a 15-year coupled control run. Pegion and Kirtman (2008) also investigate the importance of ocean–atmosphere coupling on the boreal winter ISO predictability using the NCEP operation climate model in a "perfect" model experiment. These studies are based on the hypothesis that the model is perfect, thus no model errors are considered. The potential predictability was estimated by evaluating the control simulation and the spread between different ensemble members. Previous studies described a potential predictability limit for the ISO/MJO corresponding to $\sim$15 days for precipitation and 20–30 days for circulation fields (Waliser et al. 2003; Liess et al. 2005; Fu et al. 2007; Pegion and Kirtman 2008).

However, in addition to potential predictability, there is also a need to examine the 'practical' prediction skill in coupled and uncoupled extended true-forecasts. As the dynamical models are not perfect, and include much of model errors, the practical predictability limit is expected to be far less than that of the potential predictability. For practical prediction, however, it is important to investigate how well dynamical models forecast the MJO when they include all the errors related to the dynamical model itself, as well as errors in boundary and initial conditions. Recently, Agudelo et al. (2008), using a serial extended forecast framework for boreal winter 1992/1993 with the ECMWF monthly forecast system, estimated that the overall forecast skill for circulation features (including model initial and boundary condition errors) was considerably higher than for convection-related processes with a useful (or 'practical') forecast lead time of 13 and 8 days, respectively.

It has to be emphasized that the short-term simulation characteristics may be quite different from the characteristics of long-term simulation. This is because the short-term simulation is influenced by initial conditions and is not affected as much as the long-term simulation by model biases that affect the model's capability to represent the MJO. Figure 1 shows the standard deviation of 20–100 day filtered precipitation in winter (NDJFM) for observed precipitation (CMAP, 1979–2005) and for the 20-year CGCM simulation. The coupled model is the same version used for the short-term predictions made in this paper. The long term MJO simulation variability is far weaker in intensity than that observed. However, the short-term simulations are quite different (Fig. 2). Therefore, it is useful to explore practical predictability even if the model is not perfect.

The study of Woolnough et al. (2007) is the only recent work that estimates the role of ocean–atmosphere coupling in practical prediction skill of MJO. However, their experiment is limited in the number of forecast cases,

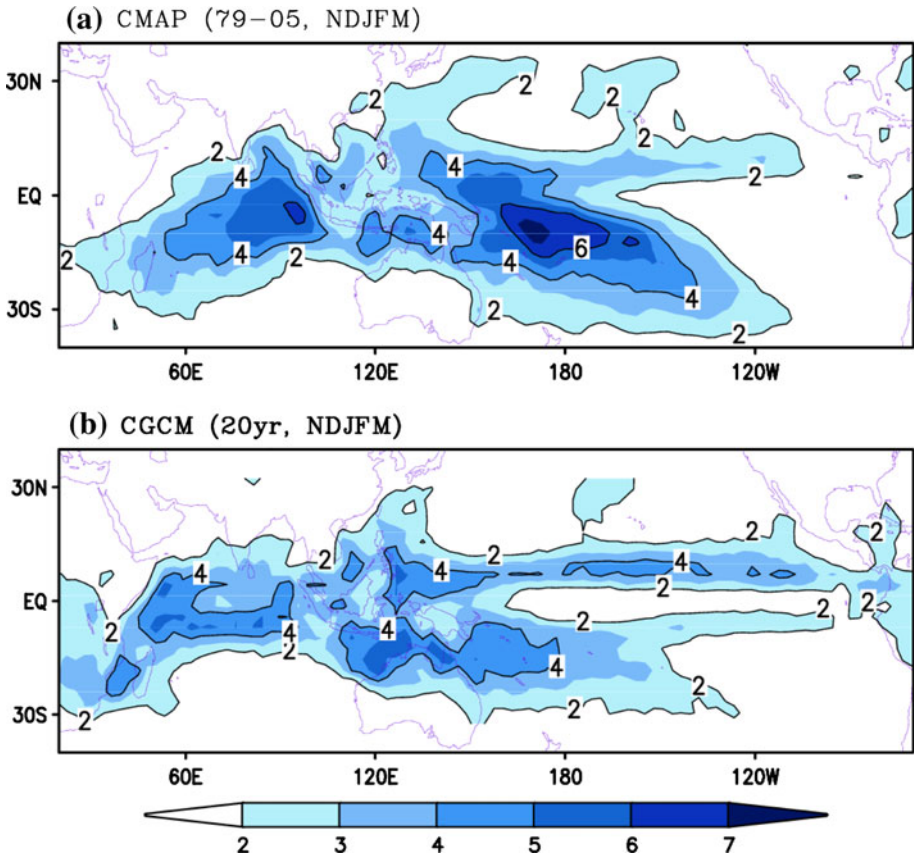

Fig. 1 Standard deviation of the 20–100 day filtered precipitation (units: mm/day) in NDJFM for **a** observed fields and **b** 20-year CGCM simulation. *Solid line* contour interval is 2 mm/day with the first contour at 2

since it only examines the winter of 1992/1993 during TOGA COARE. Previous studies revealing a dynamical MJO predictability of 7–10 days are also limited in their evaluation of forecast skill due to the length of the integrations and the number of cases explored (Chen and Alpert 1990; Lau and Chang 1992; Schemm et al. 1996; Jones et al. 2000; Seo et al. 2005). This problem is addressed in the present study by performing model experiments during 26 different boreal winters (1980–2005) similar to KHWK08.

The third distinctive difference from previous studies is the implementation of a fair comparison between the CGCM and AGCM integrations. Woolnough et al. (2007) compared the coupled model results with an experiment using persistence of the SST initial conditions. While these results provide valuable information of coupled and uncoupled models in practical prediction situations, the differences in forecasting skill between control and persistence runs cannot isolate the effect of ocean–atmosphere coupling, since they do not use the same SST as a boundary forcing. We compare the MJO simulation and forecasts in CGCM and AGCM runs by forcing the AGCM with pentad mean SSTs derived from the CGCM. Using the CGCM and AGCM with same boundary forcing, as well as the extended serial integrations framework, we can quantify the ocean–atmosphere coupling effect, not only on simulation aspects of the MJO, but also on its prediction skill. The experimental framework and information about the models used in this work are presented in Sect. 2. Results of the simulation and prediction are in Sects. 3 and 4. Section 5 provides a synthesis and a perspective of the results.

2 Experimental framework and data sources

The Seoul National University atmospheric general circulation model (SNU AGCM, Kim et al. 1998) is used in the study with a triangular truncation at wave number 42 (T42) and with 20 vertical levels. The major physical parameterizations of the model are the simplified Arakawa–Schubert scheme for convection (Moorthi and Suarez 1992), the *k*-distribution scheme for radiation (Nakajima and Tanaka 1986), a land surface model by Bonan (1998), a non-local PBL/vertical diffusion scheme (Holtslag and Boville 1993) and an orographic gravity wave drag parameterization (McFarlane 1987). Further details of the model are documented in Kim and Kang (2008). The AGCM is forced with daily SSTs interpolated from pentad mean CGCM SSTs.

The SNU coupled general circulation model (CGCM) uses the same AGCM as described above. The ocean

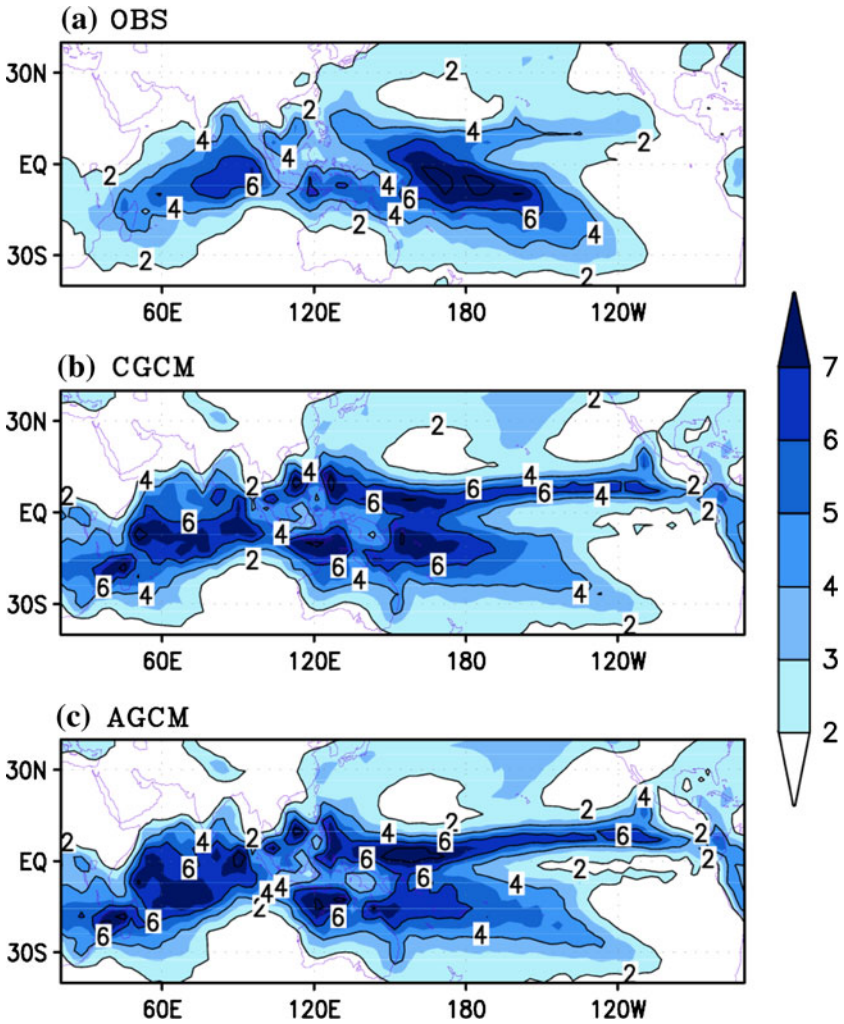

Fig. 2 Long-term time average of the standard deviation of filtered precipitation (units: mm/day) of 26 boreal winters from 1980/1981 to 2005/2006 for **a** observed fields, **b** CGCM and **c** AGCM for the entire forecast lead time. *Solid line* contour interval is 2 mm/day with the first contour at 2

component is MOM2.2 Oceanic GCM, developed by the Geophysical Fluid Dynamic Laboratory (GFDL). There are 32 vertical levels with 23 levels in the upper 450 m. A mixed layer model (Noh and Kim 1999) is embedded within the ocean model. The ocean model communicates with the atmospheric model once per day, exchanging SST, wind stress, fresh water flux, long and shortwave radiation, and turbulent fluxes of sensible and latent heat. No flux correction is applied. Details of SNU CGCM are documented in Kug et al. (2007). To obtain the initial ocean conditions, the CGCM is integrated by prescribing the salinity and temperature from NCEP Global Ocean Data Assimilation System (GODAS).

The same extended forecast experimental framework of KHWK08 (see Fig. 2 in KHWK08) is used in the present study with 30-day serial integrations across 26 boreal winters. Each experiment consists of a 30-day forecast initialized successively every 5 days (00Z) using the NCEP-NCAR reanalysis-2 as initial condition (Kanamitsu et al. 2002) for all years between 1980/1981 and 2005/2006 starting November 6. The 30-day forecast is repeated starting November 6 and every 5 days up to February 24. In total, 598 30-day serial forecasts were performed. Anomalies are calculated by removing the 26-year climatology for each 30-day forecasts at each grid point. The monthly mean OISST (Reynolds et al. 2002) is used to remove interannual variability and also to construct an ENSO index. The interannual variability associated with the ENSO index, based on a time series of NINO 3.4 SSTs, is then removed. The monthly ENSO index is interpolated to a daily time series, and a linear regression relationship is calculated with the daily fields at each grid point. Then, the ENSO-related component of each field is subtracted from the value at each grid point. Moreover, to remove further aspects of interannual variability, decadal variability and trends, a 120-day mean of the previous 120 days (including observations) is subtracted. Finally, to emphasize the intraseasonal variability, we use a 5-day moving average in each of the forecast segments to remove the high frequency variability. The days prior to the 30-day forecast are padded with two days of analyses before the moving average is applied.

The same procedure is applied to the observed fields to allow a fair comparison with experimental fields. We use velocity potential anomaly at 200 hPa (hereafter VP200) and zonal winds from the NCEP-NCAR R2, outgoing longwave radiation (OLR) from National Oceanic and Atmospheric Administration (NOAA) polar-orbiting satellites, and observed pentad mean precipitation from the Climate Prediction Center Merged Analysis of Precipitation (CMAP, Xie and Arkin 1997) that is interpolated to daily time scales. All data are interpolated to a spatial resolution of 2.8125° × 2.8125° to match the model resolution.

3 ISO/MJO simulation

3.1 Mean ISO/MJO intensity

The ISO/MJO intensity metric is the standard deviation of intraseasonally filtered precipitation calculated for both observations and simulated fields for each forecast lead time. Figure 2 shows the global distribution of the mean ISO/MJO intensity from 1-day to 30-day forecast lead times for the observation, CGCM, and AGCM runs. Overall, the largest intensity of precipitation is coincident with the regions of largest seasonal mean precipitation (e.g., Hoyos and Webster 2007) occurring over the Indian Ocean and the South Pacific Convergence Zone (SPCZ). Results from CGCM (Fig. 2b) and AGCM (Fig. 2c) show similar patterns to the observed fields as the same SST is shared among the models. But there are regional differences in amplitude in the southern part of the Indian Ocean and western Pacific. By including the ocean–atmosphere coupling processes, the ISO/MJO amplitude in SPCZ is simulated better in the CGCM with stronger variability than in the AGCM. The strong intensity in the AGCM over the Indian Ocean is weaker in the CGCM. However, the strong intensity over the western Pacific is still present in both models.

3.2 MJO propagation

Empirical orthogonal function (EOF) analysis is performed on the filtered VP200 anomalies for each forecast lead time in the tropical strip (from 40°S to 40°N) in a similar manner to KHWK08, and shows that the eastward propagating mode (MJO) is the dominant tropical ISO mode. Observations (Fig. 3a, b) show a dipole pattern in both leading EOFs with a quarter-cycle phase difference between the two principal components that represent the well-known eastward propagating pattern of the MJO (e.g. Lorenc 1984). Although there are slight differences in phase and magnitude, the pattern of the leading eigenvectors for both the uncoupled and coupled experiments is similar to observations throughout the forecast time. Therefore, only the 10-day forecast pattern is shown (Fig. 3).

Figure 4 shows the percentage of filtered variance captured by the two leading EOFs. Although the pattern of the eigenvectors is very similar (Fig. 3), the percentage of variance in each of experiment differs as the forecast lead time increases. At the beginning of the forecast, the percentage is similar to observations (about 64%). However,

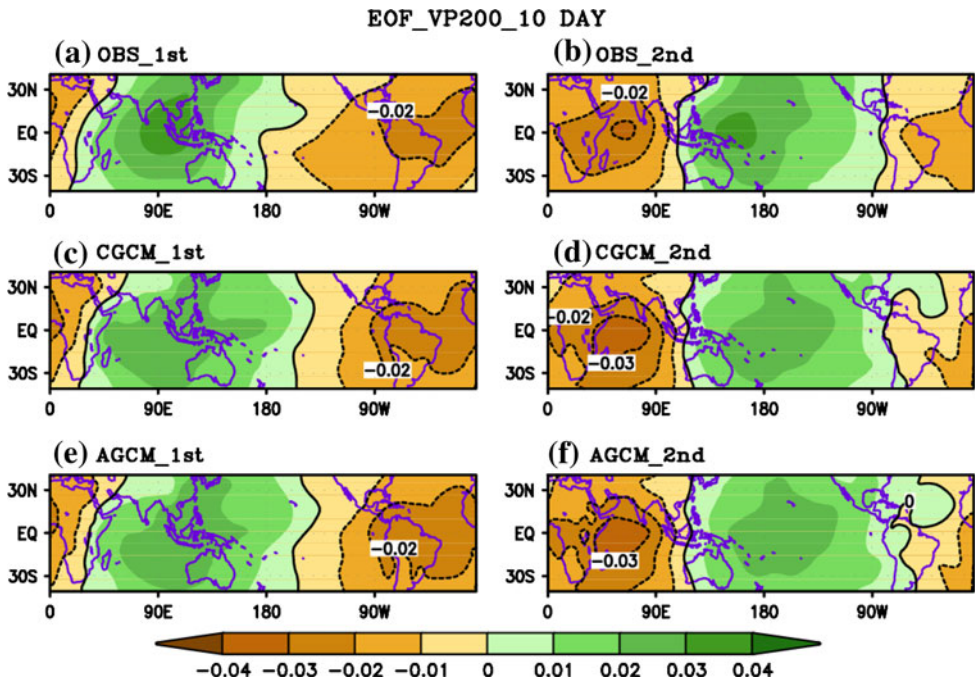

Fig. 3 The first (*left*) and second (*right*) EOF of 10-day forecast for filtered velocity potential at 200 hPa (VP200) from observed fields (*top*), CGCM (*middle*), and AGCM (*bottom*)

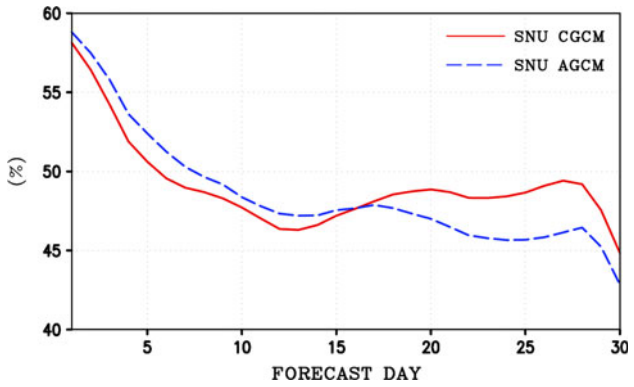

Fig. 4 Percentage of filtered variance accounted by the first two EOFs of filtered VP200 as a function of forecast lead-time for the CGCM (*solid*) and AGCM (*dashed*). The observed value is 64.3%

as the lead time increases the variance decreases gradually in both the CGCM and AGCM experiments. After day 15, though, the variance in the CGCM oscillates near 50% while the AGCM continue decreasing. These results indicate that, in spite of the similar spatial pattern of the eigenvectors in both experiments, the leading modes represent the eastward propagating MJO more clearly when the ocean–atmosphere coupling is included.

The eastward propagating nature of the MJO is manifested by a lead and lag correlation between the two principal components (PCs). Figure 5 shows the lag correlation between the PCs of the two leading modes for forecast lead times 5, 10, 15 and 20 days. The observation curve is the same for all lags and leads. At the beginning of forecast (Fig. 5a), the shape of the correlogram is very similar to observations in both experiments, with a peak when PC1 lags PC2 by 10 days (two pentads). As the forecast lead time increases (10 and 15 days) the relationship between PCs decreases in both experiments. However, the shape still indicates eastward propagation of intraseasonal anomalies in CGCM run (Fig. 5b, c). For day-20 (Fig. 5d), the correlation coefficients in the experiments are considerably lower than for the observations. The CGCM results show a slightly better result than AGCM suggesting that the ocean–atmosphere coupling improves the simulation of the eastward propagation associated with the MJO.

A wavenumber–frequency analysis is used to quantify the propagating characteristics of different modes over the tropics. In order to study further the MJO eastward propagation, the average wavenumber–frequency spectra of unfiltered VP200 anomalies, including all forecasts lead times, are examined (Fig. 6) in the same manner as in KHWK08. The spectra are computed by Fourier transforming latitudinal segments averaged between 10°S and 10°N for each year and at each forecast lead day, and then averaged over all 26-years and all forecast lead days from 1-day to 30-day. A positive (negative) zonal wavenumber means eastward (westward) propagating wave. The power in the wavenumber–frequency spectrum for observations is concentrated in the eastward propagating modes, especially in MJO timescales which is manifested as a broad peak

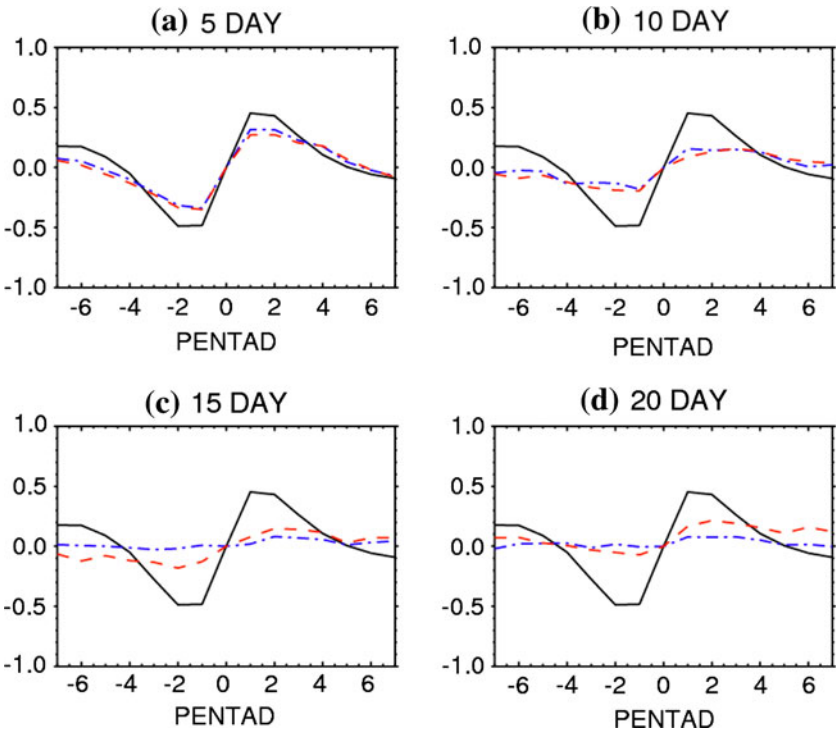

Fig. 5 Lag correlation coefficients from observations (*solid line*), CGCM (*dashed line*), and AGCM (*dashed-dot line*). A negative lag means the second principal component (PC2) leads the first (PC1)

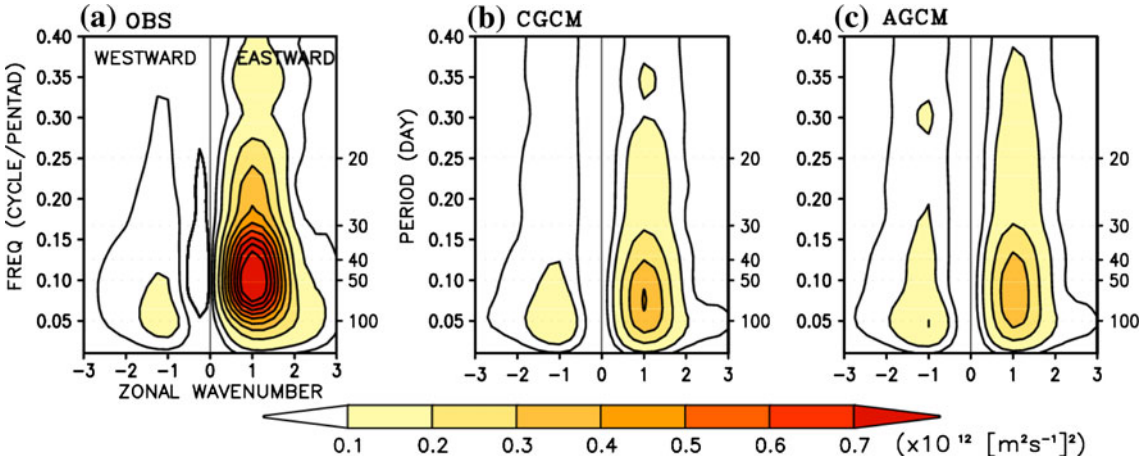

Fig. 6 Wavenumber–frequency power spectra computed for the equatorial band (10°S–10°N) for VP200 averaged from 1-day to 30-day forecasts: **a** observed, **b** CGCM, and **c** AGCM. (Units: 10^{12} m^4s^{-2})

located between 30 and 80 days and near wavenumber 1 (Fig. 6a). The spatio-temporal characteristic of eastward propagating MJO is reproduced by both experiments with weaker amplitude compared to observations (Fig. 6b, c). Although the magnitude is weaker and the peak is slightly shifted to longer periods than in the observations, the temporal and spatial scale of the CGCM experiment is in better agreement with observations than the AGCM. The difference between CGCM and AGCM is more obvious if the spectra are computed for the lead days after 15-day (not shown).

3.3 Ocean–atmosphere coupling

The weaker eastward propagating MJO of the AGCM compared to CGCM is due to the loss of a coherent evolution between convection and the underlying SST anomalies related to the MJO (e.g. Waliser et al. 1999a; Woolnough et al. 2000; Rajendran and Kitoh 2006). As in KHWK08, the limitations of improvement of MJO simulation and prediction using high frequency SSTs is caused in part by the unrealistic phase relationship between collocated convective and SSTs anomalies. In the AGCM experiment, the MJO-related fluxes have no influence on the SST and the convection adjusts to a location where the SST is most favorable, resulting in a near in-phase relationship between OLR and SST anomalies. However, in nature, the MJO variations of SST not only influence the convection and surface convergence but, at the same time, they are influenced by the atmospheric state. KHWK08 concluded that it is not possible to reproduce a realistic phase relationship by using an AGCM and suggested the problem could be overcome by including the ocean–atmosphere coupling processes.

To investigate the change of convection–SST phase relationship with increasing forecast lead time, we calculate the lagged correlation between filtered OLR and SST anomalies in a similar manner to KHWK08. Rigorously speaking, the SST anomalies are the daily mean surface temperature from the model simulation. Here, we refer to it as "SST" because the data over the ocean region is used. Correlation coefficients are calculated for each 30-day forecast. 598 30-day forecast segments (26-year × 23 segments/year) are used for obtaining the lead–lag correlation coefficients each of which consists of 29 days (−14, …, +14 day lag). Figure 7 shows the correlation coefficients as a function of forecast lead time averaged over the equatorial Indian Ocean (70°−95°E, 5°S–5°N). In the observations (Fig. 7a), the positive OLR anomalies (suppressed convection) lead enhanced SST and negative OLR (active convection) follow enhanced SST after several days.

In the CGCM experiment (Fig. 7b), the phase relationship between SST and convection is more similar to observations than in the AGCM experiment (Fig. 7c). It should be noticed that, even in the CGCM, the phase relationship does not match well with observations at the beginning of the forecast. This implies that optimal initialization, which is targeted to improve the intraseasonal phase relationships between the SST and convection, is needed for better ISO/MJO simulations. However, as the forecast lead time increases, the relationship adjusts to a quadrature phase relationship similar to that observed. A distinctive separation between negative and positive values of correlation appears after forecast day-4 (Fig. 7b). However, the AGCM shows an almost in-phase relationship through all forecast lead time (Fig. 7c). At 4-day forecast, the convection and SST show a quadrature phase relationship similar to the CGCM, but rapidly adjusts to an

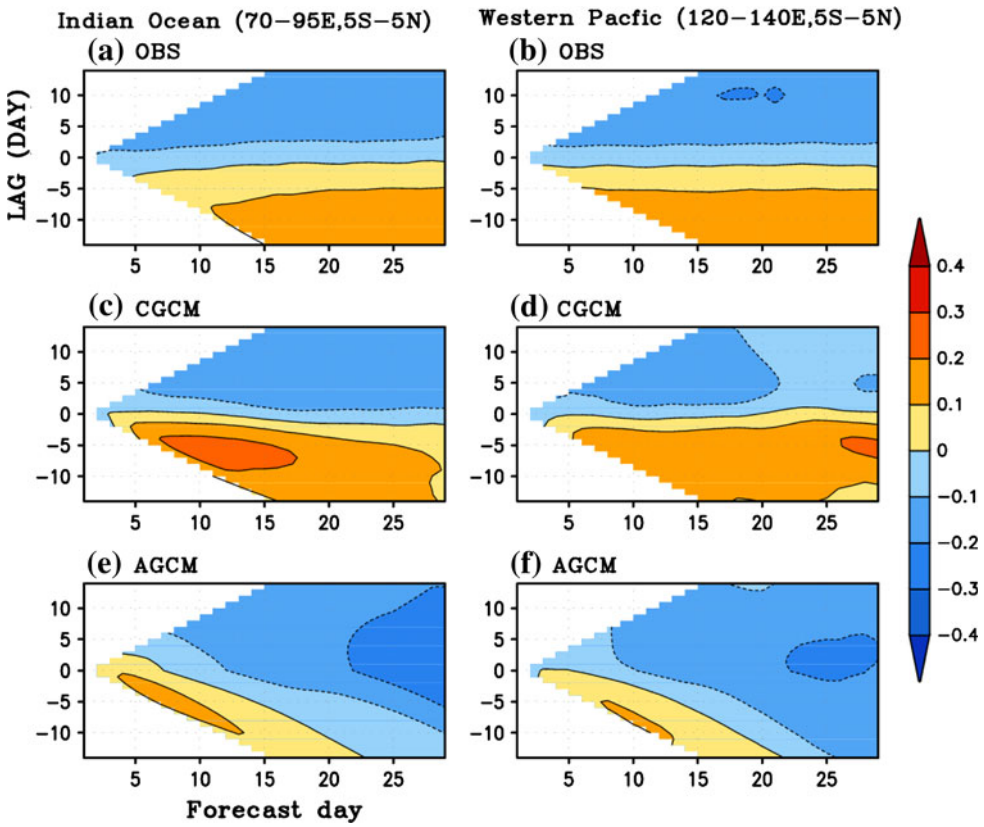

Fig. 7 Lag–correlation coefficients between filtered OLR and SST anomalies over the Indian Ocean (70°–95°E, 5°S–5°N, *left panel*) and the western pacific (120°–140°E, 5°S–5°N, *right panel*) from observations (*top*), CGCM (*middle*), and AGCM (*bottom*) as a function of forecast lead time. From the observed fields, positive SST leads enhanced convection

in-phase relationship. Similar results are observed over the western Pacific region (120°–140°E, 5°S–5°N, Fig. 7d–f). The similarity between AGCM and CGCM experiments at the beginning of the forecasts results from the direct influence of the prevailing phase relationship between atmospheric initial condition and SST boundary condition. At the beginning, the AGCM can also maintain a quadrature relationship to some extent; however, considerable differences with observations appear as the lead time increases due to the lack of ocean–atmosphere coupled processes.

4 MJO prediction

We have shown that the CGCM produces a more realistic MJO simulation compared to the AGCM in terms of the intensity, eastward propagation, and the convection–SST relationship. In this section, we will assess the impact of ocean–atmosphere coupling on the practical prediction skill using series of prediction segments.

4.1 MJO index

In previous studies of the MJO prediction, a major problem in real-time prediction is the extraction of the intraseasonally varying component without the use of time filtering. Recently, (Wheeler and Hendon (2004), hereafter WH04) developed an index for monitoring and predicting the MJO in real-time without the necessity of performing time filtering to identify the MJO features. This index is based on the combined EOFs of the observed OLR, 850 and 200 hPa zonal winds. In this study, the MJO prediction is verified using a method based on the WH04 MJO index.

The combined EOF analysis is performed using daily mean anomalies from a 28-year data from 1979 to 2006. Before conducting the EOF analysis, the seasonal cycle is removed by subtracting the time average and first three harmonics for the period of 1979–2006. Then, for removing the interannual variability, the monthly mean OISST (Reynolds et al. 2002) from 1979 to 2006 are used to construct an ENSO index (NINO 3.4 index). The interannual variability that is associated with the ENSO index is then removed. This differs from WH04, where the first rotated EOF of Indo-Pacific SSTs was used. The monthly ENSO index is interpolated to a daily basis, and linear regression relationship is calculated with the daily field at each grid point. Then, the ENSO-related component of each field is subtracted from the value at each grid point. Finally, a 120-day mean of previous 120 days is subtracted to remove further aspects of interannual variability, decadal variability and long term trends. The anomalies of the

three variables were averaged over latitudes from 15°S to 15°N and normalized by the square-root of their zonal-averaged temporal variance. Using the equatorially-averaged variables, a combined EOF analysis was performed based on the covariance matrix of the daily fields. The leading pair of principal components (PC) time series is known as the Real-time Multivariate (RMM) MJO index. The first mode is referred to as RMM1 and the second as RMM2.

Figure 8 shows the longitudinal structure of the first two combined EOFs, which describe variations associated with the MJO. The two leading modes describe 11.61 and 11.13% of the variance, respectively. The positive phase of EOF1 describes active convection over the Maritime continent region while the positive phase of EOF2 describes the suppressed convection over the Indian Ocean and active convection over the western Pacific. Observation and forecasts can be projected onto the two leading EOFs to describe the MJO phase in terms of two time series, RMM1 and RMM2. These two modes have been documented to represent the propagating nature of the MJO at different phases (WH04). Kim (2008) in Fig. 1.3 showed that these two indices are sufficient to explain much of the tropical MJO variability.

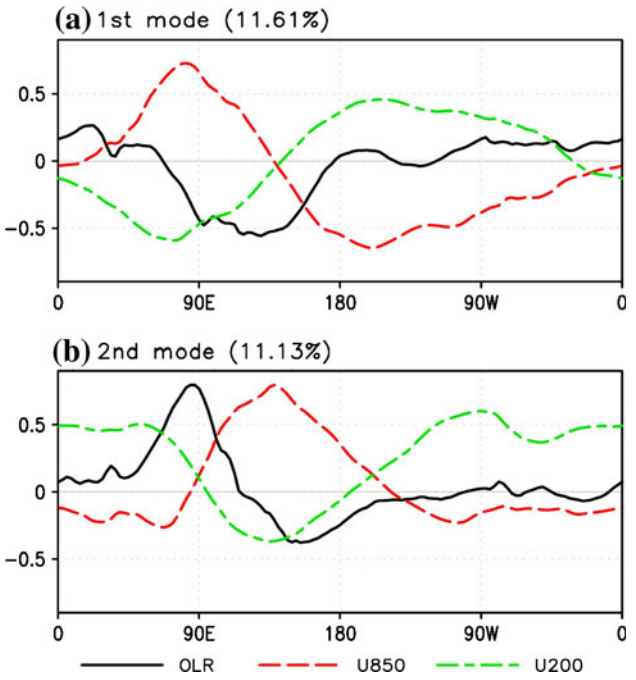

Fig. 8 Longitudinal structure of the first two combined EOFs of the OLR (*solid line*), zonal wind at 850 hPa (U850, *long dashes*), and 200 hPa (U200, *short dashes*), respectively. Each field is normalized by its global longitudinal variance before the EOF analysis. The variance explained by the respective EOFs is 11.61 and 11.13%, respectively

4.2 MJO forecast skill

In order to obtain a forecast of the MJO index, predicted zonal winds and OLR anomalies are used. The same procedure, described earlier to remove the interannual, decadal variability and trend, is performed on the model output. Using the equatorially-averaged variables, the observed combined EOF basis (Fig. 8) is projected on the predictions to obtain the leading pair of principal components (PC) time series (predicted RMM1 and 2). These indices are then rescaled to pentad resolution.

To study the extended prediction skill of the experiments, the correlation between observed and predicted RMM time series at different forecast lead days is computed (Fig. 9). The skill among experiments is very similar for forecast lead time up to 5-day with correlations in excess of 0.9 for both RMM1 and RMM2. After 10 day, the forecast skill for CGCM and the AGCM begins to separate for both RMM1 and RMM2. After the separation, the forecast skill for RMMs in the CGCM is considerably better than that in the AGCM through the remainder forecast lead time. The skill of RMM1 (RMM2) falls away rapidly to 0.5 after 17–18 (15–16) days in the AGCM and 18–19 (16–17) days in the CGCM. The skill falls continuously until the end of forecasts with higher correlations for the CGCM experiment than for the AGCM. By using the RMM as a predictand in dynamical models, Vitart et al. (2007) and Seo et al. (2009) shows that the skill of MJO is

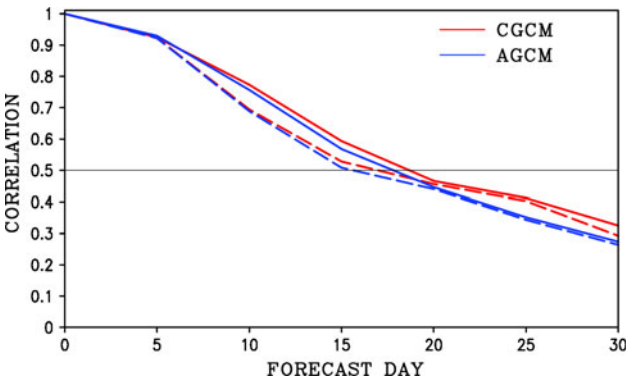

Fig. 9 Correlation coefficients between predicted and verifying values of RMM1 (*solid*) and RMM2 (*dash*) for CGCM (*red*), and AGCM (*blue*). Correlations are shown as a function of forecast lead time

near 14–15 days. Especially, Seo et al. (2009) shows the skill in dynamical prediction is nearly the same as that of the best statistical model. The forecast skill in this study is extended than previous results.

Figure 10 displays a longitude–time diagram of the filtered VP200 anomaly averaged over the tropical belt for 1992/1993 winter. The TOGA–COARE period was selected when two large MJO events occurred. We focus on the forecast starting on 31 December 1992 to make it easier to

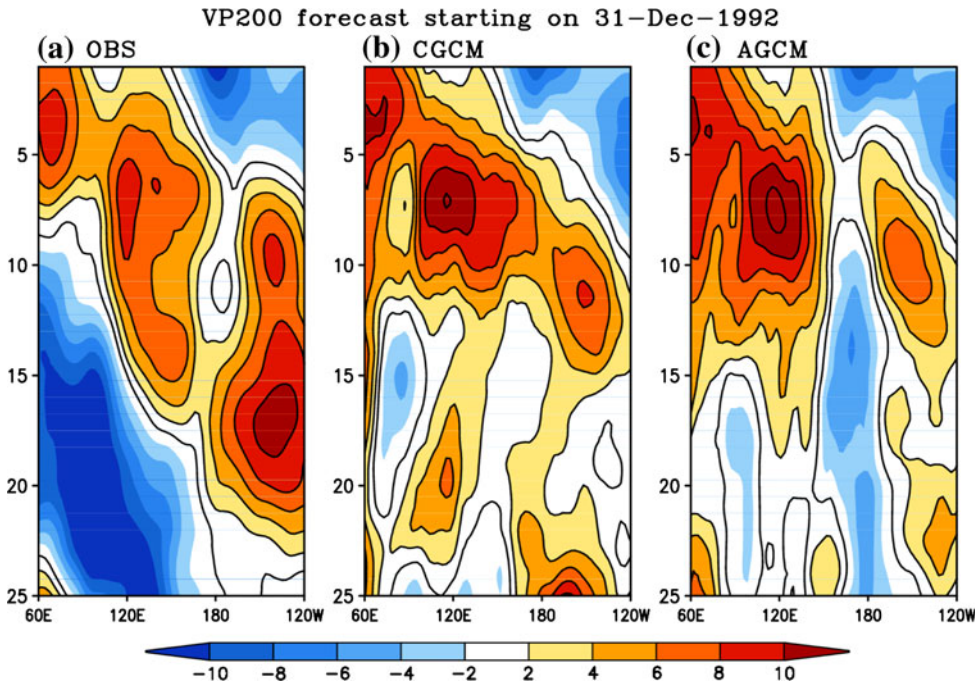

Fig. 10 Equatorial longitude–time sections of the filtered VP200 anomalies (shading interval $2 \times 10^6 m^2\ s^{-1}$) averaged across the band 10°S–10°N starting from 31 December 1992 over 25 day forecasts for **a** OBS, **b** CGCM, and **c** AGCM

compare it with previous studies (Vitart et al. 2007; Woolnough et al. 2007). Observations show (Fig. 10a), a strong MJO initiated over the Indian Ocean which moves eastward followed by, after 10–15 days, a new MJO convective initiation which also propagates eastward. The eastward propagation in both models (Fig. 10b, c) is not consistent with observations as the second convection is not predicted. However, the CGCM follows the observed propagation throughout the tropics, while the AGCM does not cross the dateline.

Improvement in the extended forecast skill in CGCM indicates the vital role for ocean–atmosphere coupling in the maintenance and propagation of the MJO. As mentioned in above and in previous studies (Fu et al. 2007; Kim and Kang 2008), the improved simulation in coupled model is most likely due to the ability to capture the interactions between the atmosphere and underlying ocean that result in a more realistic phase relationship between SST and convective anomalies. As the initial conditions are the same in both models, the additional SST–convective anomalies feedback in the CGCM extends the prediction skill compared to the AGCM.

4.3 Forecast sensitivity to the MJO initial phase

The characteristics of the amplitude and propagation during the various ISO/MJO phases are different and are likely to affect extended range forecast skill. For example, Agudelo et al. (2006) found that the extended forecast skill of the active convective periods associated with ISO is poor when initialized at the early stages of the transitional phases (break to active convection) and that the forecast skill increases substantially when the model is initialized with the correct positive lower-tropospheric moisture anomalies (late stages of the transition phase). Also, Fu et al. (2007) examined the dependence of summer ISO potential predictability on active and break phases of the ISO defined by the eastern equatorial Indian Ocean filtered rainfall anomalies. They showed the active-to-break phase is more predictable than the break-to-active phase. In addition, they showed that the minimum predictability occurs when the forecasts start from the transition phase. Both studies suggest that the phase dependence of the forecast skill should be considered in the analysis. However, previous studies of the ISO/MJO prediction have not examined the phase dependency using a comprehensive serial run experiment. In this section, we will investigate the dependency of prediction skill on the phase of MJO at the start of the forecast for both CGCM and AGCM predictions.

First, as in WH04, the RMM indices are divided by eight phases that correspond to different locations of large-scale convection over the tropics. The eight phases represent the eastward propagating MJO. For example, phase 1 represents weak convection emerging in the western Indian Ocean and dryness prevailing over the Indochina and the western Pacific. Phases 1–4 represent the developing and eastward propagating of convection over the Indian Ocean and phases 5–8 represent the eastward propagating and decaying phases over the western and central Pacific. Detail structures of each phase can be found in WH04.

The initial phase of the MJO can be determined by the RMM1 and RMM2 at the initial date of the forecast, thus all 30-day segments are classified into eight different phases for the entire 26-year forecast experiment. The number of cases for each phase is 49, 80, 86, 84, 51, 75, 82, 91, totaling 598 segments. To obtain the forecast skill of each experiment, the pattern correlation of reconstructed OLR between forecasts and observations is computed independently for each of the phases. The spatial distributions of reconstructed OLR anomalies are obtained by using the predicted RMM1 and RMM2 and the associated OLR anomaly patterns. The following formula is used for reconstruction of the OLR anomalies.

$$R-\mathrm{OLR}(x,y,t_0+\tau) = X_1(x,y)\times \mathrm{RMM1}(t_0+\tau) + X_2\mathrm{RMM2}(t_0+\tau)$$

where, R-OLR is the reconstructed OLR anomaly and X is the regressed OLR anomaly pattern onto RMM1 and RMM2. t_0 is the initial time point and τ the forecast lead time.

Figure 11 shows the prediction skill (the spatial correlation for the domain of 0°–300°E and 45°S–45°N) for different initial phases and lead times. The difference between the two forecasts skills is also presented (Fig. 11c). Until 10 days, both of the models produce a relatively high skill for phases 3 and 7 (mirror image of phase 3) and a relatively low skill for phases of 1–2 and 5–6. Phases 1–2 and 5–6 have relatively weak MJO signal when the MJO is initiated, whereas phases 3–4 and 7–8 have a large MJO signal with strong propagation over the Indian Ocean and western Pacific. This behavior is consistent with conclusions of previous studies. Specifically, using different prediction methods, previous studies have shown that the prediction skill increases if there are active ISO/MJO signals at the initial state (Lo and Hendon 2000; Jiang et al. 2008; Agudelo et al. 2008). The skill difference between CGCM and AGCM (Fig. 11c) is obvious after 15 days, especially over phases 2–4 that means the ocean–atmosphere coupling effect is crucial for the MJO over the Indian Ocean and western Pacific.

5 Discussion and conclusion

The influence of ocean–atmosphere coupling on the simulation and prediction of the boreal winter MJO has been investigated by diagnosing series of extended forecasts from 1980 to 2005 using a CGCM and an AGCM forced with pentad mean SST derived from the CGCM. By comparing both modeling experiments, which share the same atmospheric components, the impact of the ocean–atmosphere coupled process on the simulation and prediction of the MJO can be estimated rather precisely. While the mean SST is the same in both experiments, the average MJO intensity is generally closer to the observations in the CGCM experiment than in the AGCM. The ocean–atmosphere coupling acts to improve the simulation ability of the spatio-temporal evolution of the eastward propagating MJO, and the phase relationship between convection (OLR) and SST over the Equatorial Indian Ocean and the western Pacific. While the observations and the CGCM integrations exhibit a near-quadrature relationship between OLR and SST with the former lagging by about two pentads, the AGCM shows a less realistic phase relationship.

Using a serial run experiment with a large number of prediction segments and focusing specifically in large scale features of the MJO, we find a considerably longer useful forecast lead time than that of previous studies. The MJO forecast skill is especially better when ocean–atmosphere coupled processes are considered. The skill of RMM1 (RMM2) decreases to 0.5 at about 17–18 (15–16) days in the AGCM while reaching 18–19 (16–17) days in the CGCM. Improvement in forecast skill for the CGCM highlights the importance of the role of ocean–atmosphere coupling in the maintenance and propagation of the MJO. The improved simulation in coupled model is most likely due to the ability to capture the interaction between the atmosphere and the underlying ocean. As the initial conditions are the same in both models, the SST–convection anomalies feedback in the CGCM extends the prediction skill compared to AGCM. We also found the prediction

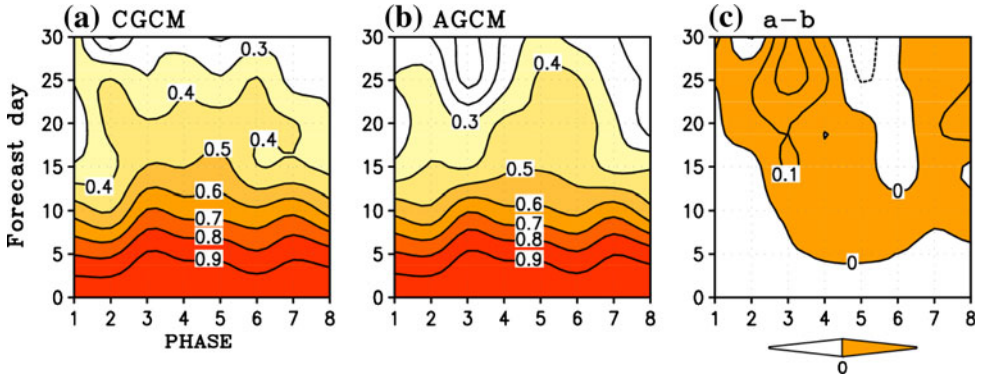

Fig. 11 Pattern correlation skill (0°–300°E and 45°S–45°N) of the reconstructed OLR anomalies for **a** CGCM, **b** AGCM, and **c** differences between CGCM and AGCM. Correlations are shown as a function of initial phase and forecast lead time. Contour interval is 0.1

skill to be phase dependent in both the CGCM and AGCM experiments. The skill is higher in CGCM when the forecasts start with MJO in the active stage.

Despite the generally poor simulation of ISO/MJO by present-day GCMs, recent studies on dynamical predictability are encouraging in terms of the overall potential for predictability. Waliser et al. (2003) found that the potential for extended predictability of precipitation anomalies associated with ISO is about 18 days. An analogous study has recently been undertaken by Liess et al. (2005) using the ECHAM AGCM, and suggest that the summer ISO has potential predictability up to 30 days. Recently, Fu et al. (2007) found the mean predictability of the summer monsoon ISO-related rainfall reaches about 24 days in the coupled model and is about 17 days in the atmosphere-only model. While the dynamical models still exhibit shortcomings in the simulation of ISO/MJO anomalies, there are possibilities for improvement in various ways to reach to the potential predictability.

Recently, Vitart et al. (2007) investigated the sensitivity of the MJO monthly forecasts to the quality of initial conditions. The intensity of MJO is significantly weaker in ERA-15 than in ERA-40. Therefore, the serial experiment using ERA-15 initial condition starts with a lower MJO signal than ERA-40. The forecast skill showed a very strong sensitivity to the quality of the atmospheric initial conditions. Previous studies have also examined the impact of the physical parameterizations on the general simulation of MJO characteristics (Wang and Schlesinger 1999; Maloney and Hartmann 2001; Lee et al. 2003). Focusing on MJO prediction, Kim 2008 investigated the prediction skill changing the convection parameterizations in 13-year serial run and found significant improvement of MJO forecasting skill using the Tokioka modification (Tokioka et al. 1988; Lee et al. 2003). Further work will address these issues.

Finally, the increase in simulation and predictive skill in a fully coupled system is not difficult to understand from a physical point of view. Stephens et al. (2004) describe the MJO as a self-regulating oscillator between the hydrological cycle and the upper ocean heating. The regulation occurs as a feedback between hydrological processes in the atmosphere; radiation processes; and the dynamical movement of air over the tropical oceans controlling variations of rainfall, cloudiness, and SST on time scales varying between 30 and 60 days. Three main phases: (1) a destabilization phase when the atmosphere becomes increasingly unstable by the combination of radiative cooling of the upper troposphere, the gradual build up of shallow convection, and the warming of the SSTs under near-clear-sky and calm conditions; (2) a convective stage where large-scale convection develops over the region resulting in widespread heavy precipitation, deepening of the oceanic mixed layer, cooling of the SST, and moistening of the upper troposphere; and (3) a restoring phase where the combination of continued cooling of the SSTs maintained by the strong low-level winds and reduced solar heating, with the radiative heating of the upper atmosphere by high clouds sustained by high humidity, are major factors in stabilizing the atmosphere, suppressing convection, bringing an end to the cooling of the SSTs, and eventually leading to a calming of the winds, dissipation of the thick upper-level clouds, and a restoration of the cycle to its warming phase. Each of these three phases are compound products of ocean–atmosphere interaction. If any of these interactions are short-circuited by, for example not allowing a full coupling between the atmosphere and the ocean, the regulation will fail and simulations and predictions will deteriorate.

Acknowledgments This research has been supported in part by Climate Dynamics Division of the United States National Sciences Foundation under Award NSF-ATM 0531771 and NOAA CPPA project NA0600AR4310005. The fourth author has been supported by the Korea Meteorological Administration Research and Development Program under Grant CATER_2006-4206 and the second stage of the Brain Korea 21 Project. Much of the work presented here was accomplished during a visit by Hye-Mi Kim to the School of Earth and Atmospheric Sciences at the Georgia Institute of Technology in 2006.

References

Agudelo PA, Curry JA, Hoyos CD, Webster PJ (2006) Transition between suppressed and active phases of intraseasonal oscillations in the Indo-Pacific warm pool. J Clim 19(21): 5519–5530

Agudelo PA, Hoyos CD, Webster PJ and Curry JA (2008) Application of a serial extended forecast experiment using the ECMWF model to interpret the predictive skill of tropical intraseasonal variability. Clim Dyn. doi: 10.1007/s00382-008-0447-x

Bergman JW, Hendon HH, Weickmann KM (2001) Intraseasonal air–sea interactions at the onset of El Nino. J Clim 14:1702–1719

Bonan GB (1998) The land surface climatology of the NCAR land surface model coupled to the NCAR Community Climate Model. J Clim 11:1307–1326

Chen TC, Alpert JC (1990) Systematic errors in the annual and intraseasonal variations of the planetary-scale divergent circulation in NMC medium-range forecasts. Mon Weather Rev 118:2607–2623

Ferranti L, Palmer TN, Molteni F, Klinker K (1990) Tropical–extratropical interaction associated with the 30–60 day oscillation and its impact on medium and extended range prediction. J Atmos Sci 47:2177–2199

Fu X, Wang B (2004a) Differences of boreal summer intraseasonal oscillations simulated in an atmosphere–ocean coupled model and an atmosphere-only model. J Clim 17:1263–1271

Fu X, Wang B (2004b) The boreal-summer intraseasonal oscillations simulated in a hybrid coupled atmosphere–ocean model. Mon Weather Rev 132:2628–2649

Fu X, Wang B, Li T, McCreary JP (2003) Coupling between northward propagation intraseasonal oscillations and sea surface temperature in the Indian Ocean. J Atmos Sci 60:1733–1753

Fu X, Wang B, Waliser DE, Tao L (2007) Impact of atmosphere–ocean coupling on the predictability of monsoon intraseasonal oscillations. J Atmos Sci 64:157–174

Han W, Lawrence D, Webster PJ (2001) Dynamical response of equatorial Indian Ocean to intraseasonal winds: zonal flow. Geophys Res Lett 28:4215–4218

Hendon HH, Liebemann B, Newman M, Glick J, Schemm JE (2000) Medium–range forecast errors associated with active episodes of the Madden–Julian oscillation. Mon Weather Rev 128:69–86

Holtslag AAM, Boville BA (1993) Local versus nonlocal boundary layer diffusion in a global climate model. J Clim 6:1825–1842

Hoyos CD, Webster PJ (2007) The role of intraseasonal variability in the nature of asian monsoon precipitation. J Clim 20:4402–4424

Jiang X, and Coauthors (2008) Assessing the skill of an all-season statistical forecast model for the Madden–Julian oscillation. Mon Weather Rev 136, 1940–1956

Jones C, Schemm JE (2000) The influence of intraseasonal variations on medium-to extended-range weather forecasts over South America. Mon Weather Rev 128:486–494

Jones C, Waliser DE, Lau WK, Stern W (2000) Prediction skill of the Madden and Julian Oscillation in dynamical extended range forecasts. Clim Dyn 16:273–289

Jones C, Waliser DE, Lau WK, Stern W (2004a) The Madden–Julian oscillation and its impact on Northern Hemisphere weather predictability. Mon Weather Rev 132:1462–1471

Jones C, Carvalho LMV, Higgins RW et al (2004b) Statistical forecast skill of tropical intraseasonal convective anomalies. J Clim 17:2078–2095

Kanamitsu M, Ebisuzaki W, Woollen J, Yang S-K, Hnilo JJ, Fiorino M, Potter GL (2002) NCEPDEO AMIP-II reanalysis (R-2). Bull Am Met Soc 83:1631–1643

Kang IS, An SI, Joung CH, Yoon SC, Lee SM (1989) 30–60 day oscillation appearing in climatological variation of outgoing longwave radiation around East Asia during summer. J Korean Meteorol Soc 25:149–160

Kang IS, Ho CH, Lim YK (1999) Principal modes of climatological seasonal and intraseasonal variations of the Asian summer monsoon. Mon Weather Rev 127:322–340

Kim HM (2008) Combined and calibrated predictions of intraseasonal variation with dynamical and statistical methods, Ph.D. Thesis, Seoul National Univ., http://hdl.handle.net/10371/763

Kim HM, Kang IS (2008) The impact of ocean–atmosphere coupling on the predictability of boreal summer intraseasonal oscillation. Clim Dyn 31:859–870

Kim JK, Kang IS, Ho CH (1998) East Asian summer monsoon simulated by the Seoul National University GCM. Proceeding on international conference on monsoon and hydrologic cycle 22:7–231

Kim HM, Kang IS, Wang B, Lee JY (2008a) Interannual variations of the boreal summer intraseasonal variability predicted by ten atmosphere–ocean coupled models. Clim Dyn 30:485–496

Kim HM, Webster PJ, Hoyos CD, Kang IS (2008b) Sensitivity of MJO simulation and predictability to sea surface temperature variability. J Clim 21:5304–5317

Kug JS, Kang IS, Choi DH (2007) Seasonal climate predictability with tier-one and tier-two prediction systems. Clim Dyn 31:403–416

Lau KM, Chan PH (1986) Aspects of the 40–50 day oscillation during the northern summer as inferred from outgoing longwave radiation. Mon Weather Rev 114:1354–1367

Lau KM, Chang FC (1992) Tropical oscillations and their predictions in the NMC operational forecast model. J Clim 5:1365–1378

Lawrence D, Webster PJ (2001) Interannual variability of intraseasonal convection and the Asian monsoon. J Clim 14:2910–2922

Lawrence DM, Webster PJ (2002) The boreal summer intraseasonal oscillation: relationship between northward and eastward movement of convection. J Atmos Sci 59:1593–1606

Lee MI, Kang IS, Mapes BE (2003) Impacts of cumulus convection parameterization on aquaplanet AGCM Simulations of tropical intraseasonal variability. J Meteorol Soc Jpn 81:963–992

Liess S, Waliser DE, Schubert S (2005) Predictability studies of the intraseasonal oscillation with the ECHAM5 GCM. J Atmos Sci 62:3320–3336

Lo F, Hendon HH (2000) Empirical extended-range prediction of the Madden–Julian oscillation. Mon Weather Rev 128:2528–2543

Madden RA, Julian PR (1972) Description of global-scale circulation cells in tropics with a 40–50 day period. J Atmos Sci 29:1109–1123

Madden RA, Julian PR (1994) Detection of a 40–50 day oscillation in the zonal wind in the tropical Pacific. Mon Weather Rev 122:813–837

Maloney ED, Hartmann DL (2001) The sensitivity of intraseasonal variability in the NCAR CCM3 to changes in convective parameterization. J Clim 14:2015–2034

McFarlane NA (1987) The effect of orographically excited gravity wave drag on the general circulation of the lower stratosphere and troposphere. J Atmos Sci 44:1775–1800

Moorthi S, Suarez MJ (1992) Relaxed Arakawa–Schubert: a parameterization of moist convection for general circulation models. Mon Weather Rev 120:978–1002

Nakajima T, Tanaka M (1986) Matrix formulation for the transfer of solar radiation in a plane-parallel scattering atmosphere. J Quant Spectrosc Radiat Transf 35:13–21

Noh Y, Kim HJ (1999) Simulations of temperature and turbulence structure of the oceanic boundary layer with the improved near-surface process. J Geophy Res 104:15621–15634

Pegion K, Kirtman BP (2008) The impact of air–sea interactions on the predictability of the tropical intraseasonal oscillation. J Clim (in press). doi: 10.1175/2008JCLI2209

Rajendran K, Kitoh A (2006) Modulation of tropical intraseasonal oscillations by ocean–atmosphere coupling. J Clim 19:366–391

Rajendran K, Kitoh A, Arakawa O (2004) Monsoon low-frequency intraseasonal oscillation and ocean–atmosphere coupling over the Indian Ocean. Geophys Res Lett 31:L02210. doi:10.1029/2003GL019031

Reynolds RW, Rayner NA, Smith TM, Stokes DC, Wang W (2002) An improved in situ and satellite SST analysis for climate. J Clim 15:1609–1625

Schemm JE, Van den Dool H, Saha S (1996) A multi-year DERF experiment at NCEP. Preprints, 11th Conf. on Numerical Weather Prediction, Norfolk, VA, Amer. Meteor. Soc., pp 47–49

Seo KH, Schemm JKE, Jones C, Moorthi S (2005) Forecast skill of the tropical intraseasonal oscillation in the NCEP GFS dynamical extended range forecasts. Clim Dyn. doi: 10.1007/s00382-005-0035-2

Seo KH, Wang W, Gottschalck J, Zhang Q, Schemm J-KE, Higgins WR, Kumar A (2009) Evaluation of MJO forecast skill from several statistical and dynamical forecast models. J Clim. doi: 10.1175/2008JCLI2421.1

Slingo JM, Rowell DP, Sperber KR et al (1999) On the predictability of the interannual behavior of the Madden–Julian Oscillation and its relationship with El Nino. Q J R Meteorol Soc 125:583–609

Stephens GL, Webster PJ, Johnson RH, Englen R, L'Ecuyer T (2004) Observational evidence for the mutual regulation of the tropical hydrological cycle and tropical sea-surface temperatures. J Clim 17:2213–2224

Tokioka T, Yamazaki K, Kitoh A, Ose T (1988) The equatorial 30–60 day oscillation and the Arakawa–Shubert penetrative cumulus parameterization. J Meteorol Soc Jpn 66:883–901

Vitart F, Woolnough S, Balmaseda MA, Tompkins AM (2007) Monthly forecast of the Madden–Julian oscillation using a coupled GCM. Mon Weather Rev 135:2700–2715

Waliser DE, Lau KM, Kim JH (1999a) The influence of coupled sea surface temperatures on the Madden–Julian oscillation: a model perturbation experiment. J Atmos Sci 56:333–358

Waliser DE, Jones C, Schemm JKE et al (1999b) A statistical extended-range tropical forecast model based on the slow evolution of the Madden–Julian oscillation. J Clim 12:1918–1939

Waliser DE, and Coauthors (2003a) AGCM simulations of intraseasonal variability associated with the Asian summer monsoon. Clim Dyn 21:423–446

Waliser DE, Stern W, Schubert S, Lau KM (2003b) Dynamic predictability of intraseasonal variability associated with the Asian summer monsoon. Q J R Meteorol Soc 129:2897–2925

Waliser DE, Murtugudde R, Lucas L (2004) Indo-Pacific Ocean response to atmospheric intraseasonal variability. Part II: Boreal summer and the intraseasonal oscillation. J Geophys Res 109. doi:10.1029/2003JC002002

Wang WQ, Schlesinger ME (1999) The dependence on convection parameterization of the tropical intraseasonal oscillation simulated by the UIUC 11-layer atmospheric GCM. J Clim 12:1423–1457

Wang B, Xie XS (1998) Coupled modes of the warm pool climate system. Part 1: the role of air–sea interaction in maintaining Madden–Julian oscillation. J Clim 11(211):6–2135

Wang B, Webster PJ, Teng H (2005) Antecedents and self-induction of active-break south Asian monsoon unraveled by satellites. Geophys Res Lett 32:L04704. doi:10.1029/2004GL020996

Webster PJ, Hoyos C (2004) Prediction of monsoon rainfall and river discharge on 15–30-day time scales. Bull Am Meterol Soc 85:1745–1765

Webster PJ, Bradley EF, Fairall CW, Godfrey JS, Hacker P, Hopuze RA Jr, Lukas R, Serra Y, Hummon JM, Lawrence TDM, Russel CA, Ryan MN, sahami K, Zuidema P (2002) The JASMINE pilot study. Bull Am Meteorol Soc 83:1603–1629

Wheeler M, Hendon H (2004) An all-season real-time multivariate MJO index: development of an index for monitoring and prediction. Mon Weather Rev 132:1917–1932

Woolnough SJ, Slingo JM, Hoskins BJ (2000) The relationship between convection and sea surface temperature on intraseasonal timescales. J Clim 13:2086–2104

Woolnough SJ, Vitart F, Balmaseda MA (2007) The role of the ocean in the Madden–Julian oscillation: implications for MJO prediction. Q J R Meteorol Soc 133:117–128

Xie P, Arkin PA (1997) Global precipitation: a 17-year monthly analysis based on gauge observations, satellite estimates, and numerical model outputs. Bull Am Meteorol Soc 78:2539–2558

Zheng Y, Waliser DE, Stern W, Jones C (2004) The role of coupled sea surface temperatures in the simulation of the tropical intraseasonal oscillation. J Clim 17:4109–4134